Yin, D., et al.,(2024). *J Env Eng Crit Chall, 3*(1):103
https://doi.org/10.33790/jeecc1100103

Journal of Environmental Engineering and Critical Challenges

Edge-Rich and Partially Oxidized WS_2 Nanodots for the Selective Detection of H_2S

Dongmin Yin[1], Xiaojie Xue[1], Juanyuan Hao[1*], and You Wang[1]
School of Materials Science and Engineering, Harbin Institute of Technology, Harbin 150001, P. R. China.

Article Details
Article Type: Research Article
Received date: 15th February, 2024
Accepted date: 09th March, 2024
Published date: 12th March, 2024

***Corresponding Author:** Juanyuan Hao, School of Materials Science and Engineering, Harbin Institute of Technology, Harbin 150001, P. R. China.

Citation: Yin, D., Xue, X., Hao, J., & Wang, Y., (2024). Edge-Rich and Partially Oxidized WS_2 Nanodots for the Selective Detection of H_2S. *J Env Eng Crit Chall, 3*(1): 103. doi: https://doi.org/10.33790/jeecc1100103.

Abstract

Tungsten disulfide (WS_2) is a promising candidate for gas sensing due to its special properties. However, the sensing response and selectivity of WS_2 based gas sensors remain to be improved. Herein, edge-rich and partially oxidized WS_2 nanodots were prepared using a fragmentation process of WS_2 powder. The optimal sensor based on these nanodots demonstrated rapid response and recovery times (20/261 s) towards 10 ppm H_2S at room temperature, with a detection limit as low as 250 ppb, excellent selectivity, and good reproducibility. The remarkable sensing performance was attributed to the synergistic effect of heterostructures and sulfur edge sites. This approach can be extended to other transition metal dichalcogenide nanomaterials to overcome their inherent challenges of slow response and incomplete recovery.

Introduction

The process of human production activities and social industrialization has brought about many problems, such as water pollution, air pollution, and extreme weather disasters. Among them, air pollution is one of the main causes of diseases and premature death. Hydrogen sulfide (H_2S), as one of the air pollutants, is a colorless, toxic, and harmful gas with a distinct rotten egg odor [1,2]. H_2S is produced in the corrosive fermentation of human solid waste and industrial production, posing various hazards to our daily production and life, such as equipment corrosion and severe poisoning [3]. As a highly toxic substance, H_2S poses significant risks to human health and the atmospheric environment. Inhalation of H_2S gas can be life-threatening, and even low concentrations can irritate the eyes, respiratory system, and central nervous system. H_2S can also cause respiratory depression, paralysis of the central nervous system for vascular movement, and other adverse reactions. Therefore, it is highly required for H_2S gas-sensitive materials with high sensitivity, low detection limits, and good selectivity.

In recent decades, sensors based on metal oxides have been widely researched for H_2S gas sensing and have shown excellent sensitivity and response. However, the use of metal oxide sensors is limited due to the requirement for high operating temperatures [4]. Two-dimensional transition metal dichalcogenides (TMDCs) have excellent optical, electrical, and mechanical properties and have potential applications in new sensing fields. Compared to graphene, two-dimensional TMDCs not only have a larger specific surface area but also have tunable bandgap structures with the number of layers. Currently, TMDC-based gas sensors have been developed for room-temperature detection of harmful gas molecules [5]. These 2D TMDCs are semiconductor materials composed of layered X-M-X sandwiches, where X represents a chalcogen element (S, Se, Te) and M represents a metal (Mo, W), providing unique properties based on tunable bandgap with the number of layers. 2D TMDC structures exhibit excellent electronic characteristics and can be applied in various fields such as water splitting, hydrogen storage, energy harvesting, optoelectronics, and gas sensors. Recent computational and experimental studies have shown that some TMDCs can effectively react with gas molecules even at ambient temperatures due to the high surface-to-volume ratio of nanosheet edges and surfaces and the presence of large active sites [6].

WS_2 is a two-dimensional layered TMDC material that has been extensively studied for gas monitoring applications. Recently, the effectiveness of p-p WS_2/CuO heterojunction prepared by Bowen Tan et al. [7] for 10 ppm NH_3 was reported to be approximately 194.9%, attributed to the improved catalytic effect of functionalized CuO nanodots on the surface of WS_2 nanosheets. Sumit Kumar et al. [8] prepared chemically exfoliated 2D quasicrystalline nanosheets and hydrothermal synthesized WS_2 nanosheets for effective NO_2 gas sensing. D. Simon Patrick et al. [9] successfully prepared WO_3/WS_2 nanocomposites through hydrothermal and annealing processes for room-temperature detection of NO_2. Jinzhu Zhang et al. [10] synthesized CdS/WS_2 composites using a hydrothermal method for room-temperature detection of NH_3. Jae-Hun Kim et al. [11] achieved CO detection using ruthenium-modified tungsten disulfide (Ru@WS_2) nanosheets. Although there have been many studies on WS_2 for gas sensors, research on WS_2 for H_2S is currently limited.

In this work, we purchased WS_2 powder with bulk structure and converted it into zero-dimensional WS_2 nanodots with abundant edge sites and partial oxidation through ultrasonic fragmentation. This conversion increases the surface adsorption active sites of the gas-sensitive material and enhances its comprehensive gas-sensing performance. The unfragmented WS_2 powder sample showed high response sensitivity to both NO_2 and H_2S (sensitivity of 3.9 to 10 ppm NO_2 and sensitivity of 4.5 to 10 ppm H_2S). By adjusting the

fragmentation time, the prepared WS_2 nanodots exhibited excellent selectivity to H_2S gas, significantly improving gas selectivity (sensitivity of 0.8 to 10 ppm NO_2 and sensitivity of 9.7 to 10 ppm H_2S). Compared to the powdered WS_2, nanoscaling the material effectively increases its specific surface area, the number of active sites, and changes the height of surface potential barriers, thickness, and effective resistance of grain, thereby greatly increasing surface activity. This allows the material to rapidly adsorb, desorb, and transfer charge carriers during gas sensing processes, resulting in higher sensitivity, shorter response time, and an expanded concentration range for gas detection.

Experimental section

Preparation of WS_2 nanodots

Tungsten disulfide (WS_2, ≥99%), Concentrated sulfuric acid (H_2SO_4, ≥98%), N-methylpyrrolidone (C_5H_9NO, ≥99%), Dimethylformamide (C_3H_7NO, 99%), ethanol (C_2H_6O, ≥99%). All chemicals were obtained commercially and used as received without further purification.

WS_2 powder (1 g) was mixed with 100 mL of N,N-dimethylformamide (DMF) in a serum bottle. The mixture was sonicated using a cell disruptor for 3 h (power of 300 W, working time of 1 s followed by a pause of 1 s for a total of 3 h) to obtain preliminary liquid-phase exfoliation of the WS_2 powder. Two-thirds of the supernatant from the preliminary exfoliation was collected and added to a three-neck flask under N_2 protection at 140 ℃ for 6 h with magnetic stirring to further exfoliate the WS_2 powder. After cooling to room temperature, the supernatant was collected using a disposable pipette and centrifuged at 2000 rpm for 5 min to remove large WS_2 flakes. The schematic diagram of WS_2 nanodots preparation process was shown in Figure S1. The resulting supernatant was transferred to a clean beaker and dried in a vacuum oven at 70 ℃ for 12 h to obtain WS_2 nanodots.

Materials characterization

Scanning Electron Microscopy (SEM) was employed to examine the morphology and surface topography of the nanodots. Transmission Electron Microscopy (TEM) allowed for analysis of the structure and size distribution of the nanodots at high resolution. X-ray Diffraction (XRD) provided information on the crystal structure and phase purity of the nanodots. Raman Spectroscopy was used to investigate the vibrational modes and molecular structure. X-ray Photoelectron Spectroscopy (XPS) helped determine the chemical composition and elemental states of the nanodots. Lastly, Ultraviolet Photoelectron Spectroscopy (UPS) provided insights into the electronic structure and valence band properties. These characterization instruments were carefully calibrated and appropriate controls and standards were employed to ensure accurate measurements and reliable data interpretation.

Gas sensing measurements

WS_2 nanodots were dispersed in ethanol to form a dispersion with a concentration of 1 mg/mL using ultrasonic treatment. WS_2 nanodot sensors were then prepared using the drop-casting method, where 20 drops of the dispersion liquid with each drop of 15 μL were deposited onto Al_2O_3 substrates with seven pairs of gold-crossed finger electrodes (50 μm gap and 50 nm thickness). The prepared sensors were exposed to a closed environment with a volume of 4 L at room temperature for static testing of their gas-sensing properties, as shown in Figure S2. A voltage of 5 V was applied to the electrode plates, and the surface current of the sensing material was measured using an electrochemical workstation (CH Instruments, 630E). To control the H_2S concentration, a syringe was used to inject 4 mL of 1000 ppm H_2S gas into the 4 L chamber, which resulted in a concentration of 1 ppm. Further injections of H_2S gas were made to establish different concentrations. The response value of the sensor was defined as "R_a/R_g," where R_a represents the resistance of the sensor in air and R_g represents the resistance in H_2S gas. The response/recovery time was calculated as the time required for the total resistance change to reach 90%.

Results and discussion

The WS_2 nanodots were prepared through sonochemical-assisted method. The size of WS_2 nanodots was controlled by adjusting the ultrasonication time. TEM images of the WS_2 powder, as well as the samples after 2 h, 3 h, and 4 h of sonication, are shown in Figure 1. The particle size of the WS_2 samples gradually decreases with increasing sonication time. The WS_2 sample sonicated for 2 h still exhibits a small flake-like structure, with a size around 100 nm. However, compared to the control group of WS_2 powder, the size of the sonicated sample has significantly reduced, along with a noticeable decrease in the number of layers. The WS_2 sample sonicated for 3 h presents a nano-dot structure, with an average particle size below 10 nm. Moreover, from the high-resolution image (Figure 1d) of the WS_2 sample sonicated for 3 h, the lattice spacing of 0.206 nm corresponds to the (006) planes of WS_2 [12], while the lattice spacing of 0.364 nm is attributed to the (200) plane of WO_3 [13]. This finding further confirms the partial oxidation of WS_2 during the sonication process, resulting in the formation of some oxidized WO_3. It is speculated that the cavitation effect during the ultrasonication process may generate localized high temperatures, leading to slight oxidation of the WS_2 material and the formation of oxidized WO_3.

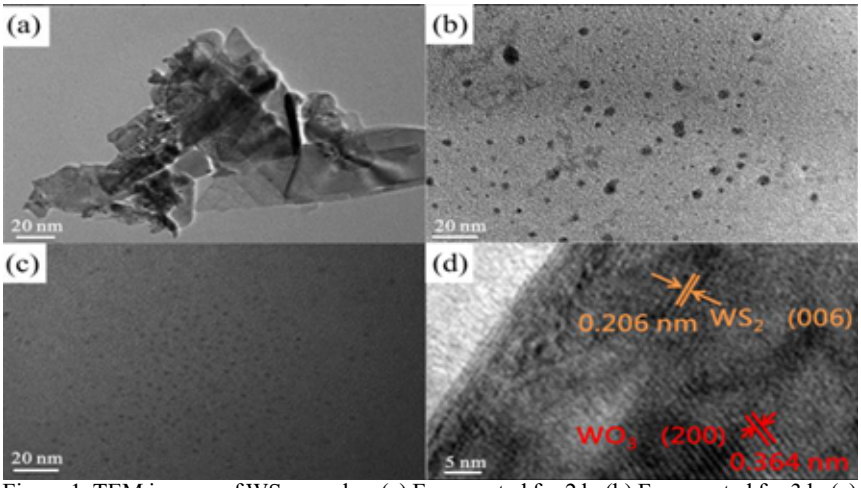

Figure 1. TEM images of WS_2 samples: (a) Fragmented for 2 h, (b) Fragmented for 3 h, (c) Fragmented for 4 h, (d) High-resolution TEM image of WS_2 fragmented for 3 h.

To understand the structural characteristics of the three sets of samples after the crushing process, XRD and Raman tests were conducted on these samples to characterize their crystal systems, crystal types, crystallinity, vibrational modes, etc., and compared them with the bulk WS_2 before crushing. The specific results are shown in Figure 2. We characterized the crystal structure of WS_2 samples with different degrees of crushing using XRD, and the results are shown in Figure 3a. By comparing the diffraction patterns in Figure 2a with the PDF standard card, it was found that the diffraction peak positions of the three sets of WS_2 samples corresponded to the positions of the diffraction peaks in JCPD Card No. 08 0237 at 14.36°, 28.94°, 32.74°, 49.73°, 58.40, and 88.52°, respectively, corresponding to (002), (004), (100), (103), (110), and (118) crystal planes. This indicates that, like the crushed WS_2 powder sample, all three sets of samples are 2H-phase WS_2 with a hexagonal crystal system, and no other impurities or components are present [14]. From the Raman spectrum in Figure 2b, it can be seen that both the pre-crushed and post-crushed WS_2 samples exhibited distinct Raman characteristic peaks at around 349 cm^{-1} and 415 cm^{-1}, which correspond to the interlayer vibration mode A_{1g} and the intralayer vibration mode E^1_{2g} of WS_2. This demonstrates that all four sets of samples are pure WS_2 phase without any other components. By comparing the Raman spectra of the crushed three sets of samples with the pre-crushed WS_2, the ratio of the integrated area of the interlayer vibration peak A_{1g} to the intralayer vibration peak E^1_{2g} of WS_2 for crushing times of 2 h, 3 h, and 4 h were 1.126, 1.367, 1.522, and 1.685, respectively. This indicates that with increasing crushing time, the proportion of interlayer vibration gradually increases, which also confirms the increase in edge sites of the samples. Additionally, it can be observed that with increasing crushing time, the A_{1g} peak and E^1_{2g} peak exhibit a redshift, demonstrating the gradual reduction in nanodot size. In conclusion, the crystal type of the WS_2 samples did not change before and after crushing. After crushing, a small amount of WO_3 was formed due to partial oxidation, and with increasing crushing time, the number of edge sites gradually increased, the particle size gradually decreased, and the number of layers in the samples also gradually decreased [15].

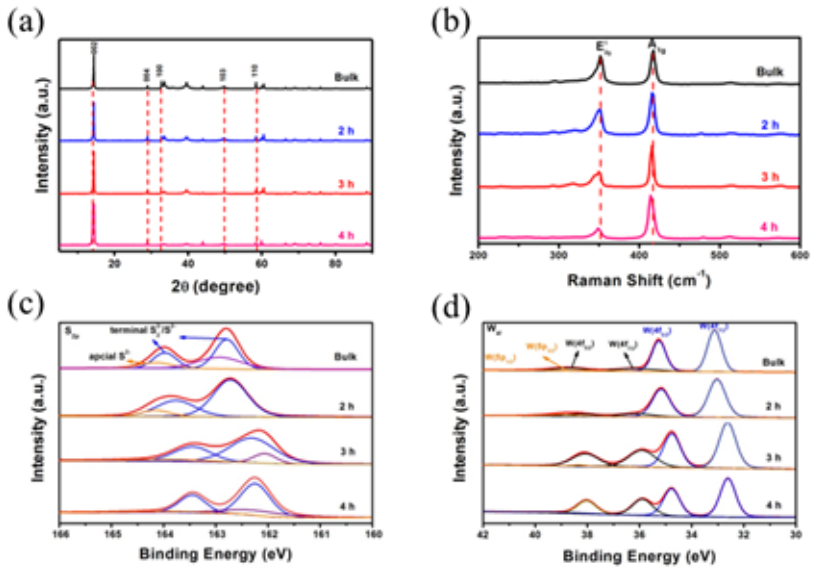

Figure 2 (a) XRD patterns, (b) Raman spectra, (c) S_2p XPS spectra, (d) W_{4f} XPS spectra of unfragmented WS_2 bulk material and WS_2 samples fragmented for different times.

The chemical composition of WS_2 before and after the fragmentation process was studied using XPS spectroscopy. Figure 2c and Figure 2d show the XPS spectra of S_{2p} and W_{4f} for four sets of samples, respectively. The characteristic peaks at 162.79 and 163.97 eV correspond to the edge S element, while the peak at 164.15 eV corresponds to the in-plane S element. The integrated area of the XPS peaks reflects the content of each element. Therefore, we integrated the peaks of the edge S and in-plane S elements for the samples and compared them. The ratio of edge S to in-plane S for the control sample WS_2 was found to be 5.8, indicating that the number of edge sites in the bulk WS_2 was relatively higher compared to the in-plane sites, but the in-plane S proportion was still high, consistent with the layered structure mentioned earlier. Using the same treatment method, the WS_2 samples with fragmentation times of 2 h, 3 h, and 4 h yielded edge S to in-plane S ratios of 8.9, 10.2, and 11.1, respectively. This indicates that as the fragmentation time increases, the number of edge S sites gradually increases, which is consistent with the Raman results mentioned earlier. As shown in Figure 3d, the characteristic peaks at 33.13, 35.26, and 38.89 eV in the fragmented WS_2 samples correspond to W^{4+} and belong to WS_2, representing $W(4f_{7/2})$, $W(4f_{5/2})$, and $W(5p_{3/2})$, respectively. The peaks at 36.13, 38.72, and 40.13 eV correspond to W^{6+} and belong to WO_3, representing $W(4f_{7/2})$, $W(4f_{5/2})$, and $W(5p_{1/2})$, respectively. This also indicates that there is partial oxidation in the control sample WS_2, but the content is minimal, which is why no corresponding diffraction peaks were observed in the XRD characterization mentioned earlier, but it is consistent with the high-resolution results. Furthermore, based on the integrated areas of W and S elements, the ratio of W to S in the control sample WS_2 was found to be 1:2. As for the WS_2 samples with fragmentation times of 2 h, 3 h, and 4 h, the ratios of W to S were found to be 1:2.11, 1:3.59, and 1:4.22, respectively. This demonstrates that as the fragmentation time increases, the number of edge S sites gradually increases, which is consistent with the XPS results of S_2p and the Raman results mentioned earlier. Additionally, the content of oxidized state WO_3 also increases with increasing fragmentation time. Moreover, it can be observed from Figure 2c and Figure 2d that with the increase in fragmentation time, both the S_{2p} peak and W_{4f} peak exhibit a certain degree of redshift, which is consistent with the redshift results mentioned earlier in Raman spectroscopy, indicating that the size of WS_2 particles gradually decreases with time [16].

In this study, we performed a screening of the most effective

dispersants and fragmentation times, with untreated WS_2 powder serving as the control group. Figure 3a and Figure 3b display the test curves of WS_2 powder after being fragmented for the same duration (3 h) in three different solvents, when exposed to 10 ppm H_2S and 10 ppm NO_2, respectively. It can be observed from the figures that the WS2 samples exhibit a p-type response to both H_2S and NO_2 gases, with dimethylformamide (DMF) showing the best fragmentation effect. The WS_2 sample fragmented in DMF achieved a sensitivity of 9.7 towards 10 ppm H_2S, along with complete recovery, while exhibiting minimal response to 10 ppm NO_2. Next, we investigated the influence of different fragmentation times on the gas sensing performance of WS_2 samples using the same dispersant, DMF. Figure 3c and Figure 3d illustrate the response of WS_2 powder fragmented for 2 h, 3 h, and 4 h in DMF, when exposed to 10 ppm H_2S and 10 ppm NO_2, respectively. It can be observed that WS_2 samples obtained after different fragmentation times all exhibited an n-type response to H_2S gas, with complete recovery, while displaying no significant response to 10 ppm NO_2. Among them, the WS_2 sample fragmented for 3 h demonstrated the optimal performance, with a sensitivity of 9.7 towards 10 ppm H_2S, whereas the WS_2 samples fragmented for 2 h and 4 h showed lower sensitivity to H_2S gas [17].

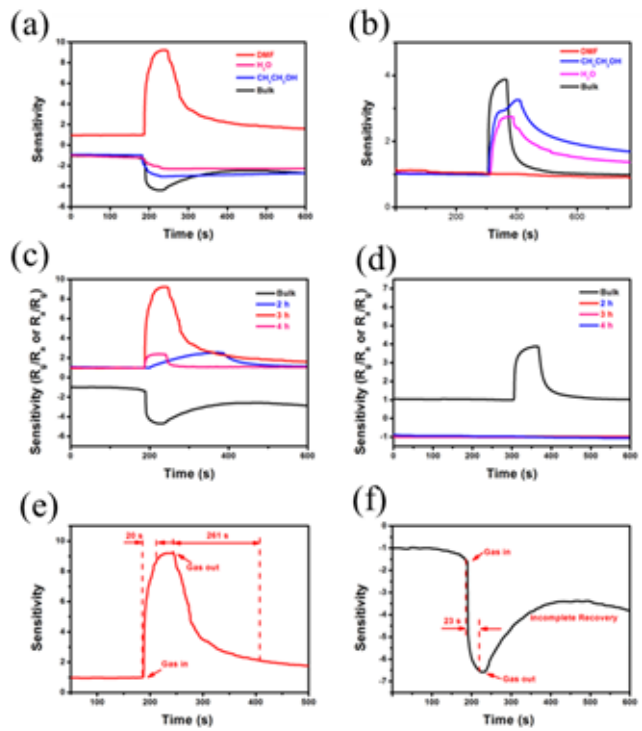

Figure 3. Response of WS_2 powder in different solvents to 10 ppm detecting gases at room temperature: (a) H_2S; (b) NO_2. Response of WS_2 powder after different fragmentation times to 10 ppm detecting gas at room temperature: (c) H_2S; (d) NO_2. (e) Response curve of WS_2 nanodots fragmented for 3 h to 10 ppm H_2S at room temperature. (f) Response curve of unfragmented WS_2 powder to 10 ppm H_2S at room temperature.

Considering the highest response value shown by the WS_2 particles after 3 h of fragmentation, further detailed research was conducted on these samples. Figure 3e and Figure 3f present the response and recovery test curves of the WS_2 sample fragmented for 3 h in DMF, along with the untreated WS_2 powder sample, when exposed to 10 ppm H_2S. The data indicates that the WS_2 sample fragmented for 3 h exhibited a response time of 20 s and a recovery time of 261 s towards 10 ppm H_2S, whereas the control group WS_2 sample had a response time of 23 s and could not completely recover. This suggests that after undergoing fragmentation, WS_2 demonstrated significantly reduced response and recovery times, making it superior in performance compared to most two-dimensional material gas sensors. These results indicate that fragmenting the samples exposes more edge sites, facilitating the transfer of charge carriers between the material and target gases, thereby achieving improvements in sensitivity, recovery rate, and recovery time [18].

Building upon the encouraging results mentioned above, the overall sensing performance of WS_2 nanodot sensors towards H_2S was systematically evaluated. In Figure 4a, the resistance curve of WS_2 nanodot sensor in response to H_2S concentrations ranging from 2 to 10 ppm was recorded. The material exhibited rapid response and recovery processes throughout the entire cyclic response, and its sensitivity increased gradually with the rise in H_2S gas concentration. Specifically, the response sensitivities of the material to 2, 4, 6, 8, and 10 ppm H_2S were found to be 4.2, 6.2, 7.6, 8.5, and 9.6, respectively. Figure 4b depicts the linear fitting curve of H_2S concentration versus response sensitivity, showing a good linear relationship between the response sensitivity of WS_2 nanodot sensor and H_2S gas concentration within the range of 2 to 10 ppm, which can be represented by the equation $y=0.66x+3.28$ with $R^2=0.97458$. The fitting curve was in good agreement with the experimental data. Furthermore, as shown in Figure 4c, the response test curves of WS_2 nanodot sensor at room temperature to 250, 500, and 750 ppb H_2S were demonstrated. The response sensitivities of the WS_2 nanodot sensor to 250, 500, and 750 ppb H_2S were measured to be 1.06, 1.16, and 1.25, indicating a high signal-to-noise ratio and suggesting that the sensor's detection limit for H_2S gas at room temperature could reach 250 ppb. It is well known that excellent selectivity and reproducibility are crucial factors for practical gas sensors. In Figure 4d, the WS_2 nanodot sensor exhibited excellent

reproducibility over five consecutive response cycles, as its response to 10 ppm NO_2 remained almost unchanged. Additionally, in Figure 4e, the response of the WS_2 nanodot sensor to 10 ppm H_2S (9.7) was significantly higher compared to its responses to 20 ppm NO_2 (0.33), NH_3 (0.88), and CH_4 (0.78), demonstrating its outstanding selectivity. Compared to the unbroken WS_2 bulk material shown in Figure 4f, the WS_2 nanodot sensor exhibited a significantly improved selectivity towards H_2S [19].

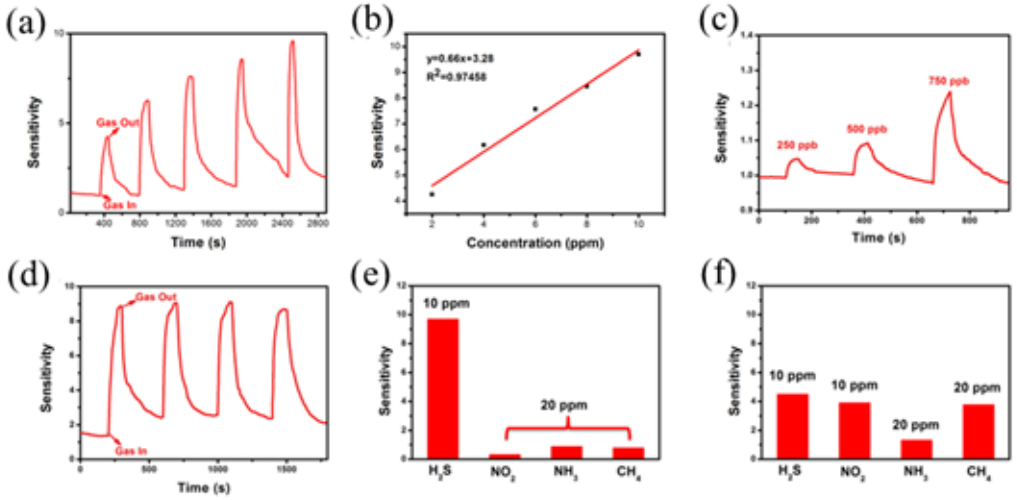

Figure 4 (a) dynamic response curve of WS_2 nanodots fragmented for 3 h, (b) linear fitting of the dynamic response curve of WS_2 nanodots fragmented for 3 h, (c) detection limit test of WS_2 nanodots fragmented for 3 h (d) stability test of WS_2 nanodots fragmented for 3 h, (e) selectivity test of WS_2 nanodots fragmented for 3 h, (f) selectivity test of unfragmented WS2 bulk material.

To further comprehensively evaluate the sensing performance of the WS_2 nanodot sensor in this study, Table 1 summarizes the comparison between our WS_2 nanodot sensor and recently reported gas sensors. It can be observed that our WS_2 nanodot sensor exhibits the best performance, confirming the high feasibility of WS_2 nanodot materials prepared through the fragmentation of WS_2 bulk material for practical H_2S detection at room temperature [20].

Sensing Materials	Sensitivity (ppm^{-1})	Working Temperature	Detection Limit (ppm)	Res./Rec. Time (s)	Ref.
WS_2 nanodots	1.0	RT	0.25	21/261	This work
NW NF WS_2	0.04	200 °C	0.20	600/900	15
NiO/WO_3	1503	100 °C	0.05	10/209	16
$SnSe_2$/WO_3	3.2	RT	0.03	136/459	17
ZnO/ZnS	32.2	100 °C	1.00	150/237	18
In_2O_3/ZnO	10.2	RT	1.00	700/600	19
NiO-CuO	4.0	RT	0.05	170/260	20

Table 1. Comparison between reports on H_2S sensor and the WS_2 sensor developed in this work

Conclusion

In conclusion, a simple experimental method of fragmenting WS_2 powder has been employed to prepare WS_2 nanodots with abundant sulfur edge sites and partial oxidation. The optimal sensor based on the nanodots exhibited rapid response/recovery (20/261 s) towards 10 ppm H_2S at room temperature, with a detection limit as low as 250 ppb, excellent selectivity, and good reproducibility. The sensing performance of our device has surpassed that of most WS_2-based sensors published before. The super sensing properties was attributed to the synergetic effect of heterostructures and the sulfur edge sites. We believe that this strategy can be generally extended to other TMD nanomaterials to address their inherent challenges of slow response and incomplete recovery.

Competing Interest: The author(s) declare that they have no competing interests.

References

1. L. He, Y. Jia, F. Meng, M. Li and J. Liu, (2009). *J Mater Sci,44*, 4326–4333.
2. F. I. M. Ali, F. Awwad, Y. E. Greish and S. T. Mahmoud, (2019). *IEEE Sensors J., 19*, 2394–2407.
3. K. Wetchakun, T. Samerjai, N. Tamaekong, C. Liewhiran, C. Siriwong, V. Kruefu, A. Wisitsoraat, A. Tuantranont and S. Phanichphant, (2011). Semiconducting metal oxides as sensors for environmentally hazardous gases, Sens. *Actuators, B*, 160, 580-591.
4. C. Wang, L. Yin, L. Zhang, D. Xiang and R. Gao, (2010). *Sensors, 10*, 2088–2106.
5. B. L. Li, J. Wang, H. L. Zou, S. Garaj, C. T. Lim, J. Xie, N. B. Li and D. T. Leong, (2016). *Adv Funct Materials, 26*, 7034–7056.

6. R. Gatensby, N. McEvoy, K. Lee, T. Hallam, N. C. Berner, E. Rezvani, S. Winters, M. O'Brien and G. S. Duesberg, (2014). *Applied Surface Science, 297*, 139–146.
7. B. Tan, R. Chen, M. He, R. Zhang, X. Lu, H. Cheng, J. Zhou and Z. Yuan, (2023). *IEEE Sensors J., 23*, 13882–13890.
8. S. Kumar, M. A. Khan, S. S. Mishra, R. Chaurasiya, N. Sharma, M. Gang, C. S. Tiwary, K. Biswas and M. Kumar, (2023). *J. Mater. Chem. C, 11*, 15119–15129.
9. D. Simon Patrick, P. Bharathi, S. Kamalakannan, J. Archana, M. Navaneethan and M. Krishna Mohan, (2024). *Applied Surface Science, 642*, 158554.
10. J. Zhang, M. Zhang, S. Wang, Z. Wu and Z. Zhang, (2023). *Langmuir, 39*, 10352.
11. J.-H. Kim, I. Sakaguchi, S. Hishita, T. Ohsawa, T. T. Suzuki and N. Saito, (2022). *Sensors and Actuators B: Chemical, 370*, 132454.
12. Xiaoyang Duan, DanXu, Wenjun Jia, Bohao Sun, Ran Li, Ruitian Yan and Wenjie Zhao, (2024). *Nanoscale, 16*, 2478.
13. Xiaoyang Duana, Dan Xua, Wenjun Jia, Ran Li, Bohao Sun, Ruitian Yan and Wenjie Zhao, (2024). *Sensors & Actuators: A. Physical, 365*, 114854.
14. Sumit Kumar, Mustaque A. Khan, Shashank Shekhar Mishra, Rajneesh Chaurasiya, Nipun Sharma, Meng Gang, Chandra S. Tiwary, Krishanu Biswas and Mahesh Kumar, (2023). *J. Mater. Chem. C, 11*, 15119
15. G. A. Asres, J. J. Baldoví, A. Dombovari, T. Järvinen, G. S. Lorite, M. Mohl, A. Shchukarev, A. Pérez Paz, L. Xian, J.-P. Mikkola, A. L. Spetz, H. Jantunen, Á. Rubio and K. Kordás, (2018). *Nano Res., 11*, 4215–4224.
16. D. Feng, L. Du, X. Xing, C. Wang, J. Chen, Z. Zhu, Y. Tian and D. Yang, (2021). *ACS Sens., 6*, 733–741.
17. X. Guo, Y. Ding, C. Liang, B. Du, C. Zhao, Y. Tan, Y. Shi, P. Zhang, X. Yang and Y. He, (2022). *Sensors and Actuators B: Chemical, 357*, 131424.
18. X. Wu, Z. Zhao, L. Zhang and W. Jiao, (2022). *Semicond. Sci. Technol., 37*, 085017.
19. M. Sun, H. Yu, X. Dong, L. Xia and Y. Yang, (2020). *Journal of Alloys and Compounds, 844,* 156170.
20. Y. Ding, Q. Zhuang, X. Guo, H. Li, C. Liang, B. Du, C. Zhao, Y. Shi, G. Meng, R. Li, Z. Zang and Y. He, (2023). *Applied Surface Science, 612*, 155792.